

Unsupervised Discovery of Object-Centric Neural Fields

Rundong Luo ^{*1} Hong-Xing Yu ^{*1} Jiajun Wu ¹

Abstract

We study inferring 3D object-centric scene representations from a single image. While recent methods have shown potential in unsupervised 3D object discovery from simple synthetic images, they fail to generalize to real-world scenes with visually rich and diverse objects. This limitation stems from their object representations, which entangle objects' intrinsic attributes like shape and appearance with extrinsic, viewer-centric properties such as their 3D location. To address this bottleneck, we propose the unsupervised discovery of Object-Centric neural Fields (uOCF). uOCF focuses on learning the intrinsics of objects and models the extrinsics separately. Our approach significantly improves systematic generalization, thus enabling unsupervised learning of high-fidelity object-centric scene representations from sparse real-world images. To evaluate our approach, we collect three new datasets, including two real kitchen environments. Extensive experiments show that uOCF enables the unsupervised discovery of visually rich objects from a single real image, allowing applications such as 3D object segmentation and scene manipulation. In particular, uOCF demonstrates zero-shot generalization to unseen objects from a single real image. Project page: <https://red-fairy.github.io/uOCF/>.

1 Introduction

Creating factorized, object-centric 3D scene representations is a fundamental ability in human vision and a long-standing topic of interest in computer vision and machine learning. Some recent work has explored unsupervised learning of 3D factorized scene representations from images alone (Stelzner et al., 2021; Yu et al., 2022; Smith et al., 2023; Jia et al., 2023). These methods have delivered promising results in 3D object discovery and reconstruction from a simple synthetic image.

^{*}Equal contribution. ¹Stanford University.

However, difficulties arise when attempting to generalize these approaches to complex real-world scenes. The bottleneck lies in their object representations: they represent each object in the viewer's frame, entangling intrinsic object attributes such as shape and appearance with extrinsic properties such as the object's 3D location. Such a paradigm means that a slight shift in the object's location or a subtle camera adjustment can significantly change its latent representation. Intuitively, an object's intrinsic attributes should remain consistent irrespective of location, yet this invariance is ignored in existing 3D object-centric learning models. As demonstrated by convolutional networks (Zhang, 2019), accounting for this invariance is crucial for generalization (Chattopadhyay et al., 2020; Deng et al., 2022). The entanglement of object intrinsics and extrinsics substantially hinders sample efficiency and systematic generalization.

We propose the unsupervised discovery of Object-Centric neural Fields (uOCF), which learns to infer 3D object-centric scene representations from a single image. Unlike existing methods, uOCF focuses on learning the intrinsics of objects and models the extrinsics separately. As shown in Figure 1, uOCF generalizes to unseen real-world scenes. We train uOCF on sparse multi-view images without object annotations. During inference, uOCF takes a single image and generates a set of object-centric neural radiance fields and a background radiance field.

Our translation-invariant design facilitates learning object priors from scenes with different compositional configurations (*e.g.*, the number of objects and spatial arrangements) and allows learning from multiple different data sources. For example, uOCF can learn object priors from single-object room scenes and generalize to multi-object kitchen scenes with unknown spatial layouts. Moreover, such generalization even facilitates *zero-shot* 3D object discovery on real images with unseen objects.

To evaluate our approach, we introduce new challenging datasets for 3D object discovery, including two real kitchen datasets and a synthetic room dataset. The two real datasets feature varied kitchen backgrounds and objects from multiple categories. The synthetic room dataset features chairs with diverse, realistic shapes and textures. Across all these datasets, uOCF offers high-fidelity discovery of object-centric neural fields, allowing applications such as unsu-

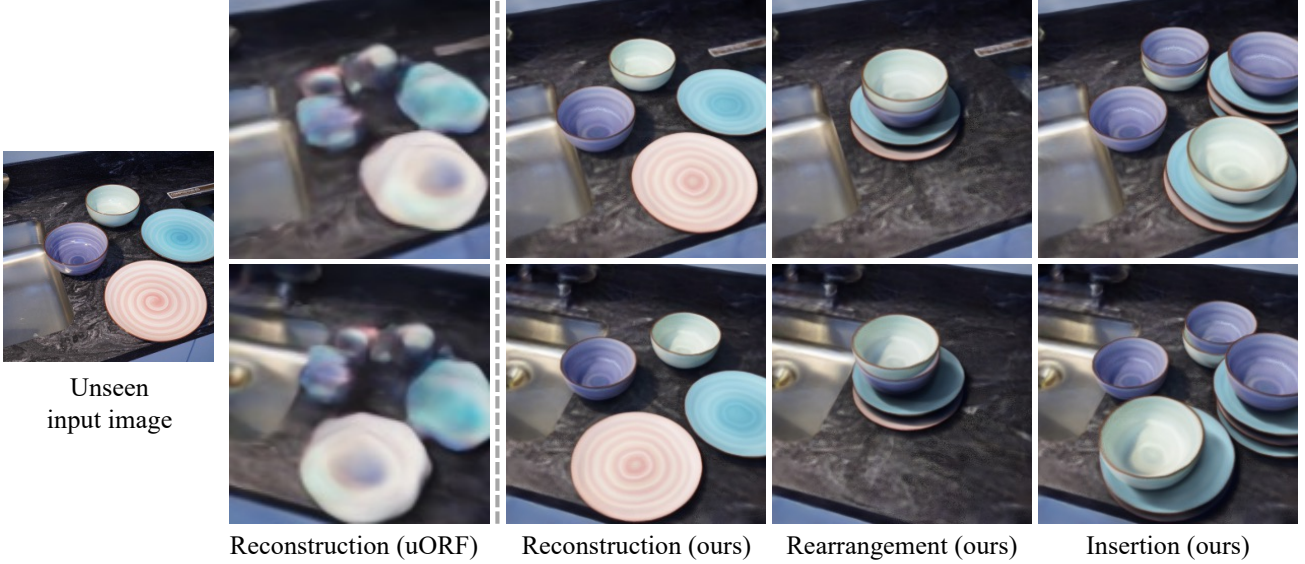


Figure 1: We propose the unsupervised discovery of Object-Centric neural Fields (uOCF), which infers factorized 3D scene representations from an unseen real image, thus enabling scene reconstruction and manipulation from novel views. We compare uOCF with the state-of-the-art method, uORF (Yu et al., 2022).

pervised 3D object segmentation and scene manipulation from a real image.

In summary, our contributions are threefold:

- First, we highlight the overlooked role of object-centric modeling in unsupervised 3D object discovery. We instantiate the idea by proposing the unsupervised discovery of Object-Centric neural Fields (uOCF).
- Second, we introduce the object-centric prior learning technique, which leverages uOCF’s translation-invariant property to learn object priors from scenes with different object-compositional configurations.
- Lastly, we collect three challenging datasets, Room-Texture, Kitchen-Matte, and Kitchen-Shiny, and show that uOCF significantly outperforms existing methods on these datasets, unlocking zero-shot, single-image object discovery.

2 Related Works

Unsupervised Object Discovery. Prior to the rise of deep learning, traditional methods for object discovery (often referred to as co-segmentation) primarily aimed at locating visually similar objects across a collection of images (Sivic et al., 2005; Russell et al., 2006), where objects are defined as visual words or clusters of patches (Grauman & Darrell, 2006; Joulin et al., 2010). This clustering concept was later incorporated into deep learning techniques for improved grouping results (Li et al., 2019; Vo et al., 2020). The incorporation of deep probabilistic inference propelled the field towards factorized scene representation learning (Eslami et al., 2016). These methods decompose a visual scene into

several components, where objects are often modeled as latent codes that can be decoded into image patches (Kosiorek et al., 2018; Crawford & Pineau, 2019; Jiang et al., 2020; Lin et al., 2020), scene mixtures (Greff et al., 2016; 2017; 2019; Burgess et al., 2019; Engelcke et al., 2019; Locatello et al., 2020; Biza et al., 2023; Didolkar et al., 2023), or layers (Monnier et al., 2021). Despite their efficacy in scene decomposition, they do not model the objects’ 3D nature.

To model the 3D nature of scenes and objects, some recent works tried to learn 3D-aware representations from multi-view images of a single-scene (Liang et al., 2022) or of large datasets for generalization (Eslami et al., 2018; Chen et al., 2020; Sajjadi et al., 2022), while the latest research emphasizes the single-image inference of object-centric factorized scene representations (Stelzner et al., 2021; Yu et al., 2022; Smith et al., 2023). Notably, Yu et al. (2022) propose the unsupervised discovery of object radiance fields (uORF) from a single image. Later literature improves the efficiency (Smith et al., 2023) and segmentation (Jia et al., 2023). However, their object representations suffer from extrinsic entanglement and limited generalizability to complex scenes. In contrast, our approach explicitly disentangles object appearances from their extrinsics.

Object-Centric 3D Reconstruction. Decomposing visual scenes on an object-by-object basis and estimating their semantic/geometric attributes has been explored in several recent works (Wu et al., 2017; Yao et al., 2018; Kundu et al., 2018; Ost et al., 2021). Some approaches, like AutoRF (Müller et al., 2022), successfully reconstruct specific objects (*e.g.*, cars) from annotated images. Others decompose visual scenes into the background and individual ob-

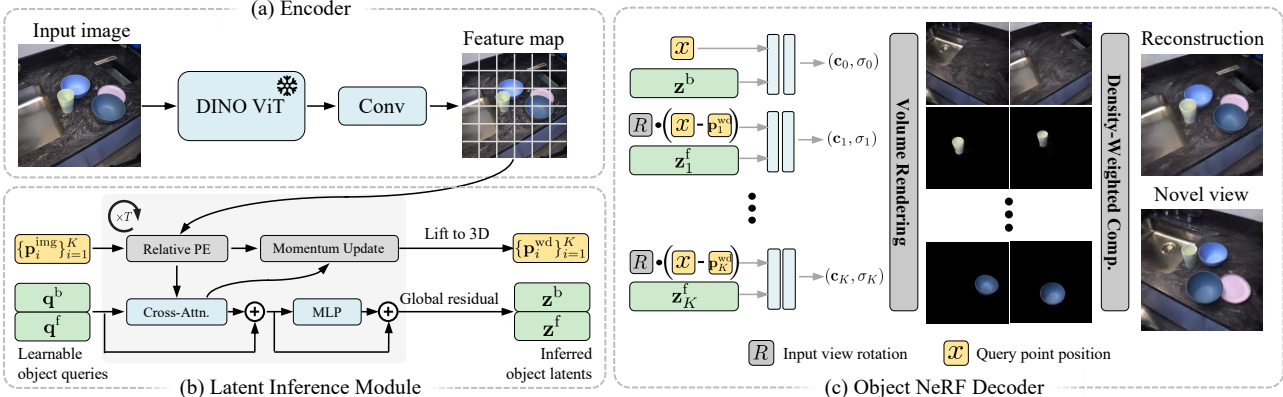


Figure 2: With a single forward pass, uOCF processes a single image input to infer a set of object-centric radiance fields along with their 3D locations and background radiance field. uOCF is trained on sparse multi-view images from a collection of scenes and uses a single image as input during inference.

jects represented by neural fields (Yang et al., 2021; Wu et al., 2022). Our work differs as it emphasizes unsupervised learning. Another line of recent work focuses on lifting 2D segmentation to reconstructed 3D scenes, such as Fan et al. (2022); Cen et al. (2023a;b). In contrast, our work aims at single-image inference, whereas these studies concentrate on multi-view reconstruction.

Generative Neural Fields. Neural fields have revolutionized 3D scene modeling. Early works have shown promising geometry representations (Sitzmann et al., 2019; Park et al., 2019). The seminal work by Mildenhall et al. (2020) on neural radiance fields has opened up a burst of research on neural fields. We refer readers to recent survey papers (Tewari et al., 2020; Xie et al., 2022) for a comprehensive overview. Particularly, compositional generative neural fields such as GIRAFFE (Niemeyer & Geiger, 2021) and others (Nguyen-Phuoc et al., 2020; Wang et al., 2023b) also allow learning object representations from image collections. Yet, they target unconditional generation and cannot tackle inference.

3 Approach

Given a single input image, our goal is to infer object-centric radiance fields (*i.e.*, each discovered object is represented in its local object coordinate rather than the world or the viewer coordinates) and the objects’ 3D locations. The object-centric design not only boosts generalizability due to representation invariance but also allows learning object priors from scenes with different spatial layouts and compositional configurations. The following provides an overview of our approach and then introduces the technical details.

3.1 Model Overview

As shown in Figure 2, uOCF’s architecture consists of an encoder, a latent inference module, and a decoder.

Encoder. From an input image \mathbf{I} , the encoder extracts a feature map $\mathbf{f} \in \mathbb{R}^{N \cdot C}$, where $N = H \cdot W$ is the spatial

size of the feature map and C represents the number of channels. We set it as a frozen DINOv2-ViT (Oquab et al., 2023) followed by two convolutional layers.

Latent Inference Module. The latent inference module infers the latent representation and position of the objects in the underlying 3D scene from the feature map. We assume that the scene is composed of a background environment and no more than K foreground objects. Therefore, the output includes a background latent $\mathbf{z}^b \in \mathbb{R}^{1 \times D}$ and a set of foreground object latent $\mathbf{z}^f = [\mathbf{z}_1^{fT} \mathbf{z}_2^{fT} \dots \mathbf{z}_K^{fT}]^T \in \mathbb{R}^{K \times D}$ with their corresponding positions $\{\mathbf{p}_i^{\text{wd}}\}_{i=1}^K$, where $\mathbf{p}_i^{\text{wd}} \in \mathbb{R}^3$ denotes a position in the world coordinate. Note that some object latent may not represent any object when the scene has fewer than K objects.

Decoder. Our decoder employs the conditional NeRF formulation $g(\mathbf{x}|\mathbf{z})$, which takes the 3D location \mathbf{x} and the latent \mathbf{z} as input and generates the radiance color and density for rendering. We use two MLPs, g^b and g^f , for the background environment and the foreground objects, respectively.

3.2 Object-Centric 3D Scene Modeling

Object-Centric Latent Inference. Our Latent Inference Module (LIM) aims at binding a set of learnable object queries ($\mathbf{q}^f = [\mathbf{q}_1^{fT} \mathbf{q}_2^{fT} \dots \mathbf{q}_K^{fT}]^T \in \mathbb{R}^{K \times D}$) to the visual features of each foreground object, and another query to the background features ($\mathbf{q}^b \in \mathbb{R}^{1 \times D}$). The binding is modeled via the cross-attention mechanism with learnable linear functions $\mathcal{K}^b, \mathcal{K}^f, \mathcal{Q}^b, \mathcal{Q}^f, \mathcal{V}^b, \mathcal{V}^f$:

$$\mathbf{A}_{i,j} = \frac{\exp(\mathbf{M}_{i,j})}{\sum_k \exp(\mathbf{M}_{i,k})}, \text{ where} \\ \mathbf{M} = \frac{1}{\sqrt{D^s}} \left[\mathcal{Q}^b(\mathbf{q}^b) \cdot \mathcal{K}^b(\mathbf{f})^T \quad \mathcal{Q}^f(\mathbf{q}^f) \cdot \mathcal{K}^f(\mathbf{f})^T \right]^T \in \mathbb{R}^{N \times (K+1)}. \quad (1)$$

We then calculate the update signals for queries via an attention-weighted mean of the input:

$$\begin{aligned}\mathbf{u}^b &= (\mathbf{W}_{(:,1)})^T \cdot \mathcal{V}^b(\mathbf{f}) \in \mathbb{R}^{1 \times D}, \\ \mathbf{u}^f &= (\mathbf{W}_{(:,2)})^T \cdot \mathcal{V}^f(\mathbf{f}) \in \mathbb{R}^{K \times D},\end{aligned}\quad (2)$$

where $\mathbf{W}_{i,j} = \frac{\mathbf{A}_{i,j}}{\sum_t \mathbf{A}_{t,j}}$ is the attention map normalized over the spatial dimension. Queries are then updated by:

$$\begin{aligned}\mathbf{q}^b &\leftarrow \mathbf{q}^b + \mathbf{u}^b, \quad \mathbf{q}^f \leftarrow \mathbf{q}^f + \mathbf{u}^f, \\ \mathbf{q}^b &\leftarrow \mathbf{q}^b + t^b(\mathbf{q}^b), \quad \mathbf{q}^f \leftarrow \mathbf{q}^f + t^f(\mathbf{q}^f),\end{aligned}\quad (3)$$

where t^b and t^f are MLPs. We repeat this procedure for T iterations, followed by concatenating the updated object queries with the corresponding attention-weighted mean of the input feature map \mathbf{f} (global residual), finally delivering the background latent \mathbf{z}^b and foreground latent $\{\mathbf{z}_i^f\}_{i=1}^K$.

Our LIM is related to the Slot Attention (SA) (Locatello et al., 2020) while differs in several critical aspects. We discuss their relationship in Appendix C.1.

Position Inference in 2D. To infer objects’ position along with their latent representation, we assign a normalized image position $\mathbf{p}_i^{\text{img}} \in [-1, 1]^2$ initialized as zero to each foreground query, then iteratively update them by momentum m with the attention-weighted mean over the normalized 2D grid $\mathbf{E}^{\text{abs}} \in [-1, 1]^{N \times 2}$:

$$\mathbf{p}_i^{\text{img}} \leftarrow (\mathbf{W}_{(:,i+1)})^T \cdot \mathbf{E}^{\text{abs}} \cdot (1 - m) + \mathbf{p}_i^{\text{img}} \cdot m. \quad (4)$$

To incorporate the inferred positions, we adopt the relative positional encoding (Biza et al., 2023) $\mathbf{E}_i^{\text{pos}} := \text{concat}([\mathbf{E}^{\text{abs}} - \mathbf{p}_i^{\text{img}}, \mathbf{p}_i^{\text{img}} - \mathbf{E}^{\text{abs}}]) \in \mathbb{R}^{N \times 4}$, where concat is the concatenation along the last dimension. Then, we re-write M in Eq. (1) as:

$$M = \frac{1}{\sqrt{D^s}} \begin{bmatrix} \mathcal{Q}^b(\mathbf{q}^b) \cdot \mathcal{K}^b(\mathbf{f} + h_1(\mathbf{E}^{\text{abs}}))^T \\ \mathcal{Q}^f(\mathbf{q}_1^f) \cdot \mathcal{K}^f(\mathbf{f} + h_1(\mathbf{E}_1^{\text{pos}}))^T \\ \dots \\ \mathcal{Q}^f(\mathbf{q}_K^f) \cdot \mathcal{K}^f(\mathbf{f} + h_1(\mathbf{E}_K^{\text{pos}}))^T \end{bmatrix}^T, \quad (5)$$

where $h_1 : \mathbb{R}^4 \rightarrow \mathbb{R}^D$ is a linear function.

Overall, LIM achieves a gradual binding between the queries and the objects in the scene through an iterative update of the queries and their locations. To address potential issues of duplicate object identification, we invalidate one of two similar object queries with high similarity and positional proximity by the start of the last iteration. Finally, a small bias term is added to the position to handle potential occlusion, *i.e.*, $\mathbf{p}_i^{\text{img}} \leftarrow \mathbf{p}_i^{\text{img}} + \tanh(h_2((W_{(:,i+1)})^T)) \cdot \alpha$, where scaling hyperparameter $\alpha = 0.2$ and $h_2 : \mathbb{R}^N \rightarrow \mathbb{R}^2$ is a linear function.

Lifting Position to 3D. The 2D positions $\mathbf{p}_i^{\text{img}}$ are then unprojected into the 3D world coordinate to obtain \mathbf{p}_i^{wd} . We consider two scenarios: for objects on a known shared plane (*e.g.*, using plane detection (Ge et al., 2023)), a direct ray extension (extend the ray between the camera center and $\mathbf{p}_i^{\text{img}}$ to intersect the ground plane) is used; alternatively, in the absence of such a plane, we extend the rays by depth $d \cdot s_i$, where d is the distance between the camera and the scene center and $\{s_i\}_{i=1}^K$ are scaling terms predicted by a linear layer using the camera parameters and object latent as input. These two approaches are referred to as uOCF-P and uOCF-N, respectively, with uOCF denoting uOCF-P by default. Further details and visualizations of these processes are provided in Appendix C.1.

Compositional Neural Rendering. The object positions allow us to put objects in their local coordinates rather than the viewer or world coordinates, thereby obtaining object-centric neural fields. Technically, for each 3D point \mathbf{x} in the world coordinate, we transform it to the i^{th} object’s local coordinate by $\mathbf{x}_i = R \cdot (\mathbf{x} - \mathbf{p}_i^{\text{wd}})$, where R denotes the input camera rotation matrix. We then retrieve the color and density of \mathbf{x} in the foreground radiance fields as $(\mathbf{c}_i, \sigma_i) = g^f(\mathbf{x}_i | \mathbf{z}_i^f)$ and in the background radiance field as $(\mathbf{c}_0, \sigma_0) = g^b(\mathbf{x} | \mathbf{z}^b)$. These values are aggregated into the scene’s composite density and color $(\bar{\sigma}, \bar{\sigma})$ using density-weighted means:

$$\bar{\sigma} = \sum_{i \geq 0} \omega_i \sigma_i, \quad \bar{\mathbf{c}} = \sum_{i \geq 0} \omega_i \mathbf{c}_i, \quad \text{where } \omega_i = \frac{\sigma_i}{\sum_{j \geq 0} \sigma_j}. \quad (6)$$

Finally, we compute the pixel color by volume rendering. Our pipeline is trivially differentiable, allowing backpropagation through all parameters simultaneously.

Discussion on Extrinsics Disentanglement. An object’s canonical orientation is ambiguous without assuming its category (Wang et al., 2019). Thus, we choose not to disentangle objects’ orientation since we target category-agnostic object discovery. Further, we observe that uOCF has learned meaningful representations that can smoothly interpolate an object’s scale and orientation. Please refer to Appendix B for visualization and analysis.

3.3 Object-Centric Prior Learning

Unsupervised 3D object discovery in complex compositional scenes is inherently difficult due to ambiguities. For example, when an object is partially occluded with a visually similar object, the inference model needs to find the object boundary to separate the occluded one from the blocker and generate plausible completion to the occluded object.

One way to address such a challenge is to learn object priors. However, existing methods have difficulties learning generalizable object priors, as their object representation is sensitive to spatial configurations: a minor shift in camera

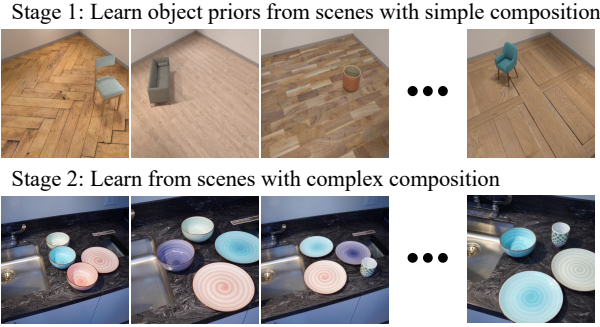


Figure 3: Our object-centric design allows learning object priors from scenes with different compositional configurations. We first train our model on simple configurations (*e.g.*, scenes with a single synthetic object) to learn *category-agnostic* object priors. Then, we adapt this prior to complex scenes. Note that no object annotation is needed in either stage.

pose or object location, rather than the object itself, can lead to drastic changes in the object representation. Thus, such learned object priors do not generalize when there are unseen spatial configurations. Our 3D object-centric representation mitigates this issue due to its translation-invariance.

Therefore, we introduce object-centric prior learning. The main idea is to learn general object priors (*e.g.*, physical coherence) from simple scenes (*e.g.*, scenes with a single synthetic object), then leverage the obtained priors to learn from more complex scenes that could potentially have very different scene geometry and spatial layout. We show an illustration in Figure 3.

3.4 Model Training

Object-Centric Sampling. To improve the reconstruction quality, we leverage an object’s local coordinates to concentrate the sampled points in proximity to the object, as illustrated in Figure 10(b). Specifically, we start dropping distant samples from the predicted object positions after a few training epochs when the model has learned to distinguish the foreground objects and predict their positions. This approach enables us to quadruple the number of samples with the same amount of computation, leading to significantly improved robustness and visual quality.

In both training stages, we train our model across scenes, each with calibrated sparse multi-view images. For each training step, the model receives an image as input, infers the objects’ latent representations and positions, renders multiple views from the input and reference poses, and compares them to the ground truth images to calculate the loss. Model supervision consists of the MSE reconstruction loss ℓ_{recon} and the perceptual loss ℓ_{perc} (Johnson et al., 2016) between the reconstructed and ground truth images. In addition, we incorporate the depth ranking loss (Wang et al., 2023a) with pre-trained monocular depth estimators and background occlusion regularization (Yang et al., 2023) to



Figure 4: Samples from our datasets.

minimize common floating artifacts in few-shot NeRFs.

The overall loss function is thus formulated as follows:

$$\mathcal{L} = \ell_{\text{recon}} + \lambda_{\text{perc}} \ell_{\text{perc}} + \lambda_{\text{depth}} \ell_{\text{depth}} + \lambda_{\text{occ}} \ell_{\text{occ}}. \quad (7)$$

4 Experiments

We evaluate our method on unsupervised object segmentation in 3D, novel view synthesis, and scene manipulation in 3D. Please refer to Appendix D for limitation analysis and Appendix E for more experimental results.

Data. We curate two real-world datasets to evaluate our method and one synthetic dataset for learning object priors.

Room-Texture. The synthetic dataset includes 324 object models from the “armchair” category of the ABO (Collins et al., 2022) dataset. Each scene contains one object set against a background randomly chosen from a collection of floor textures. We also render a multi-object variant with 2-4 objects in each scene to promote comparison with existing methods. The single-object subset contains 1296 scenes, and the multi-object subset contains 5000 scenes for training and 100 for evaluation. Each scene is rendered from 4 directions toward the scene center.

Kitchen-Matte. This dataset features scenes with single-color matte dinnerware and two kinds of background environments: plain tabletop and complex kitchen backdrop. There are 735 scenes for training and 102 for evaluation. Each scene contains 3-4 objects at random positions and is captured from 3 poses (for tabletop scenes) or 2 poses (for kitchen backdrops).

Kitchen-Shiny. This dataset comprises scenes with textured shiny dinnerware. Similar to Kitchen-Matte, the first half presents a plain tabletop, while the latter has a complex kitchen background. There are 324 scenes for training and 56 for evaluation.

Figure 4 shows some samples drawn from our datasets, and more details on data collection are provided in Appendix C.2.

Details on the Object-Centric Prior Learning. In our experiments, we first train our model on synthetic room scenes with only one chair. This synthetic data is easy to generate and scale up. We empirically find that despite the

Table 1: Scene segmentation and novel view synthesis result on Room-Texture. Baseline methods are uORF (Yu et al., 2022), BO-QSA (Jia et al., 2023), and COLF (Smith et al., 2023).

Method	Scene segmentation			Novel view synthesis		
	ARI↑	FG-ARI↑	NV-ARI↑	PSNR↑	SSIM↑	LPIPS↓
uORF (Yu et al., 2022)	0.670	0.093	0.578	24.23	0.711	0.254
BO-QSA (Jia et al., 2023)	0.697	0.354	0.604	25.26	0.739	0.215
COLF (Smith et al., 2023)	0.235	0.532	0.011	22.98	0.670	0.504
uOCF-N (ours)	0.791	0.584	0.722	28.81	0.796	0.138
uOCF-P (ours)	0.785	0.563	0.704	28.85	0.798	0.136

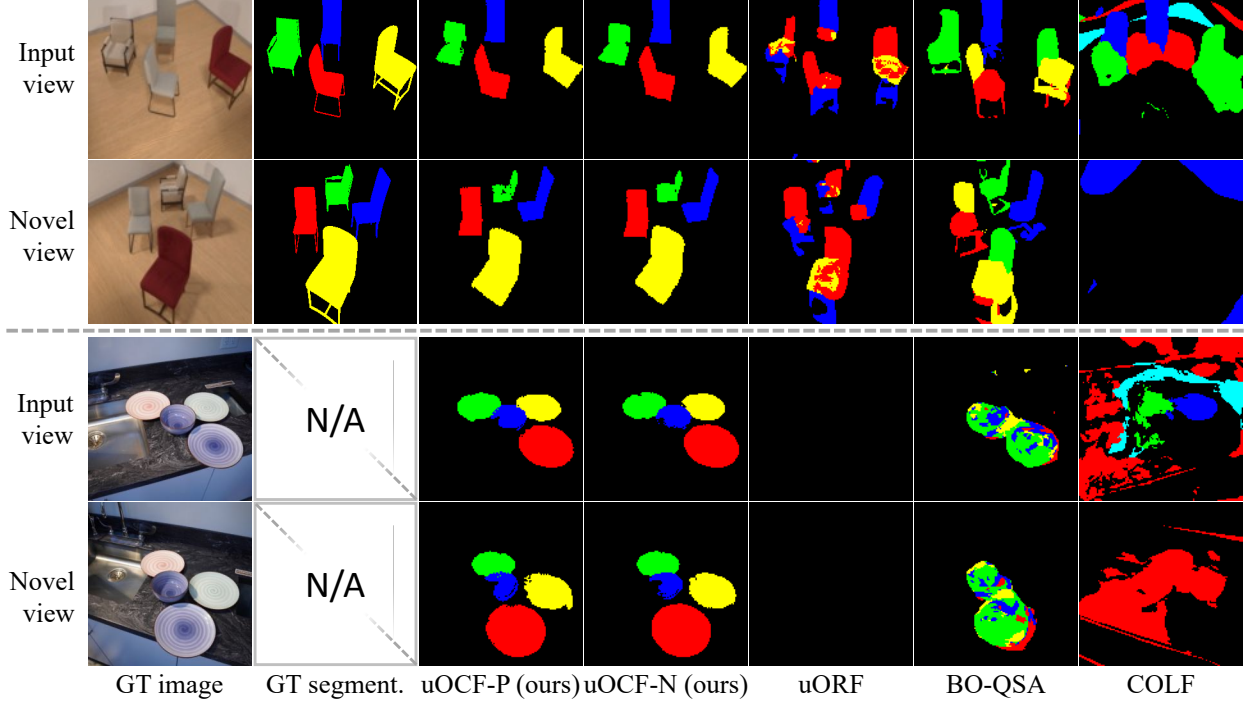


Figure 5: Scene segmentation qualitative results. Novel view images are for reference only.

domain gap, uOCF can learn category-agnostic object priors to generalize to different object categories. The object priors learned from synthetic chairs effectively apply to dinnerware in real kitchen scenes. Further experimental evidence can be found in Appendix E.1, where we show that this technique is effective even when object priors are learned from simple CLEVR shapes (monochromatic primitives like cubes and spheres) (Johnson et al., 2017).

Qualitative Metrics. We report the PSNR, SSIM, and LPIPS metrics for novel view synthesis. For scene segmentation, we use three variants of the Adjusted Rand Index (ARI): the conventional ARI (calculated on all input image pixels), the Foreground ARI (FG-ARI, calculated on foreground input image pixels), and the Novel View ARI (NV-ARI, calculated on novel view pixels). All scores are computed on images of resolution 128×128 .

Baselines. We compare our method with uORF (Yu et al., 2022), BO-QSA (Jia et al., 2023), and COLF (Smith et al., 2023). During testing, the model uses a single image with

known camera intrinsics as input and outputs the reconstruction/segmentation results from target poses. We increase the latent dimensions and training iterations for the baselines for fair comparisons. By default, we set the number of foreground object queries to $K = 4$ across all methods and discuss its effect in Appendix E.1. Further details on experimental configuration are provided in Appendix C.3.

4.1 Unsupervised Object Segmentation in 3D

We begin our evaluation by object segmentation. We render a density map \mathbf{d}^i for each latent i and assign each pixel p a segmentation label $s_p = \arg \max_{i=0}^K \mathbf{d}_p^i$.

The results are presented in Table 1 and Figure 5. On synthetic Room-Texture scenes, our method outperforms existing methods in all metrics. Notably, no baseline method can produce reasonable segmentation results in real-world Kitchen-Shiny scenes. Specifically, uORF binds all objects to the background, resulting in empty object segmentation; BO-QSA fails to distinguish different object in-

Table 2: Novel view synthesis results on Kitchen-Shiny and Kitchen-Matte.

Method	Kitchen-Shiny			Kitchen-Matte		
	PSNR↑	SSIM↑	LPIPS↓	PSNR↑	SSIM↑	LPIPS↓
uORF (Yu et al., 2022)	19.23	0.602	0.336	26.07	0.808	0.092
BO-QSA (Jia et al., 2023)	19.78	0.639	0.318	27.36	0.832	0.067
COLF (Smith et al., 2023)	18.30	0.561	0.397	20.68	0.643	0.236
uOCF-N (ours)	27.87	0.842	0.055	28.25	0.841	0.055
uOCF-P (ours)	28.58	0.862	0.049	29.40	0.867	0.043

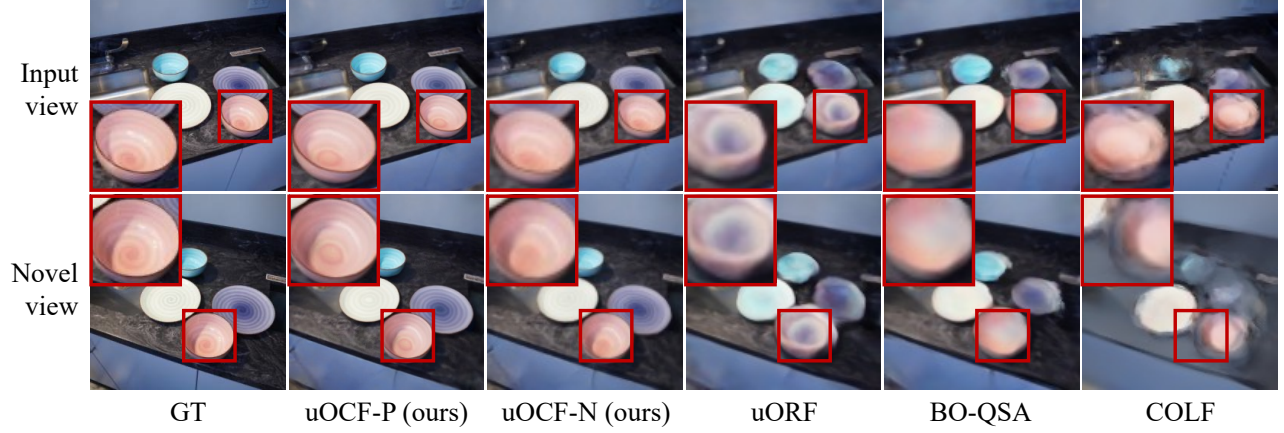


Figure 6: Novel view synthesis qualitative results on Kitchen-Matte (top rows) and Kitchen-Shiny (bottom rows).

Table 3: Quantitative scene manipulation results on Room-Texture.

Method	PSNR↑	SSIM↑	LPIPS↓
Object Translation			
uORF	23.65	0.654	0.284
BO-QSA	25.21	0.700	0.226
uOCF-N (ours)	27.70	0.773	0.156
uOCF-P (ours)	27.66	0.774	0.156
Object Removal			
uORF	23.81	0.664	0.282
BO-QSA	24.58	0.698	0.247
uOCF-N (ours)	29.20	0.803	0.132
uOCF-P (ours)	28.99	0.802	0.136

stances; COLF produces meaningless results on novel views as light fields do not guarantee multi-view consistency. In contrast, thanks to object-centric modeling, uOCF better distinguishes the foreground objects and consistently produces satisfactory scene segmentation results, demonstrating its effectiveness in object-centric representation learning. Moreover, uOCF can handle scenes in which objects occlude each other. Please see Appendix E.4 for more results.

4.2 Novel View Synthesis

Evaluation then proceeds to novel view synthesis. For each test scene, we use a single image as input and the remaining images as references.

The results are shown in Table 2 and Figures 6, 19, 20. Our method significantly surpasses baselines across all metrics.

Importantly, while previous methods often fail to distinguish foreground objects and thus produce messy results, our approach consistently produces high-fidelity scene reconstruction and novel view synthesis results.

4.3 Scene Manipulation in 3D

This section evaluates uOCF’s ability in scene manipulation. Being able to infer objects’ positions, uOCF readily supports the following scene editing functions: 1) object translation, achieved by modifying the object’s position sent to the decoder, and 2) object removal, achieved by excluding certain objects during compositional rendering. In the following, we first quantitatively evaluate uOCF on the Room-Texture dataset, followed by qualitative evaluations on the real-world Kitchen-Shiny dataset.

Quantitative Evaluation. On the Room-Texture dataset, we randomly select an object within the scene and relatively shift its position (object translation) or remove it (object removal). We render images from four viewpoints for every scene, along with the ground truth mask of the altered object. During testing, we determine the object to manipulate by selecting the object with the highest IoU score with the ground truth mask. Note that while existing methods are limited to relative position adjustment, our approach uniquely allows absolute translations due to the disentanglement of object positions and representations. As shown in Table 3, uOCF outperforms baselines across all metrics, justifying its effectiveness in scene manipulation.

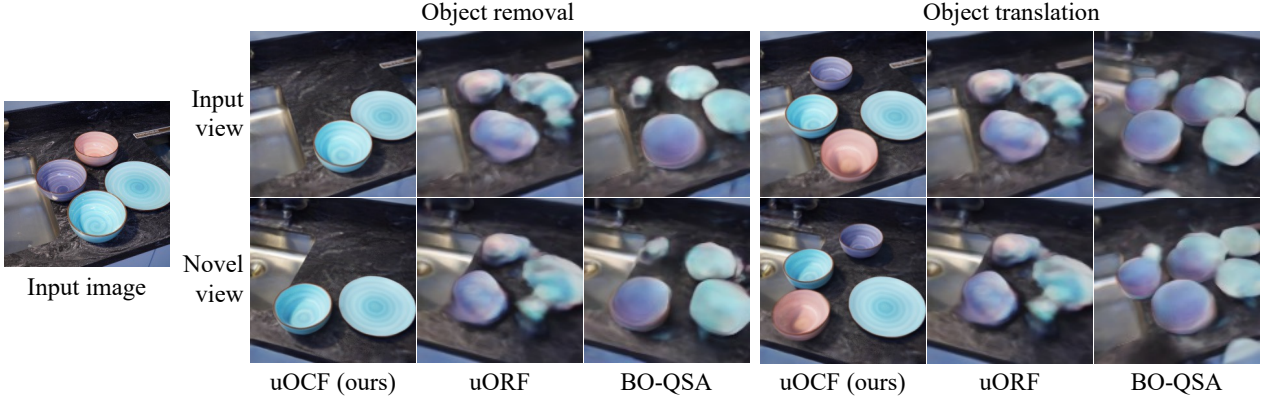


Figure 7: Qualitative results of single-image 3D scene manipulation. The three bowls’ positions are shifted for object translation.

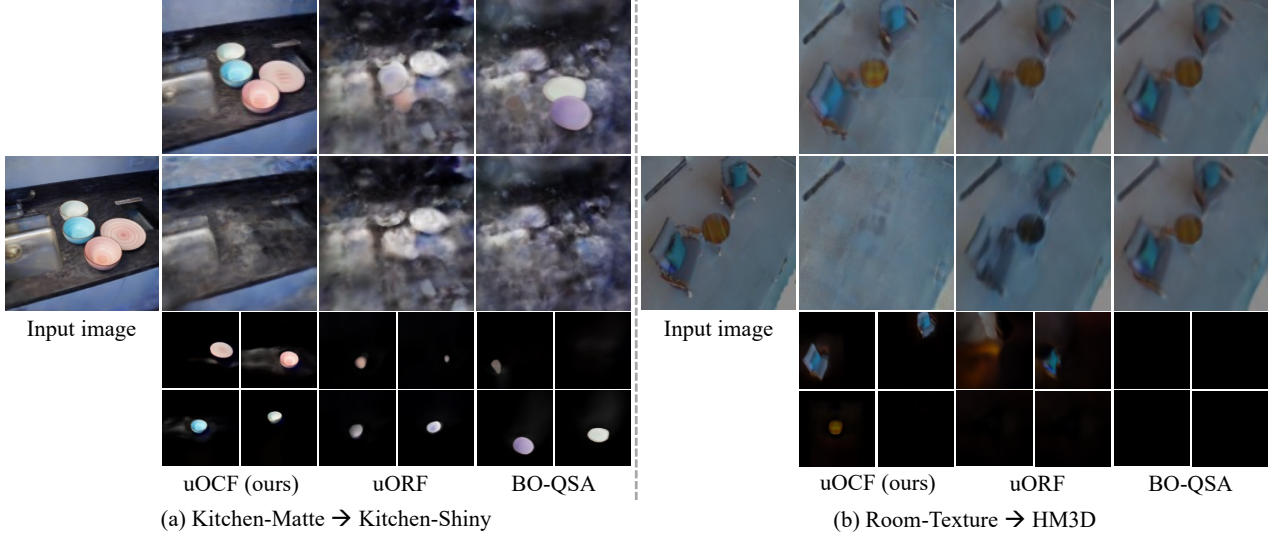


Figure 8: Zero-shot generalization results. We load the model trained on one dataset and test it on an image from another more complex dataset with a fast test-time optimization. First/second/third row: scene/background/object reconstruction.

Qualitative Evaluation. Figure 7 offers the qualitative scene manipulation results on the Kitchen-Shiny dataset. As shown, uORF merges all objects into the background, making scene manipulation unfeasible (hence, the manipulation results are identical to the original reconstructions); BO-QSA fails to distinguish foreground objects correctly, resulting in messy manipulation results (see Figure 17 for a visual breakdown of each object latent). In contrast, uOCF delivers much more reasonable and visually satisfactory results than previous methods. Please refer to the supplementary video for additional visualization results.

4.4 Generalization Analysis

Finally, we explore the zero-shot generalizability of uOCF, where we adapt the model trained on Kitchen-Matte to an unseen scene in Kitchen-Shiny through a fast test-time optimization. We also try to adapt the model trained on Room-Texture to an unseen scene from the indoor scan dataset, HM3D (Ramakrishnan et al., 2021). Note that only one image is used instead of multi-view images. As shown in

Figure 8, whereas previous methods struggle to generalize to unseen objects or fail to separate foreground objects from the background, uOCF demonstrates outstanding generalizability, only requiring a fast test-time optimization to generalize from one dataset to new, more complex objects.

We also explore the few-shot setting, where the model is trained with 10/50/100 scenes instead of the whole dataset. Please refer to Appendix E.3 for results and analysis.

5 Conclusion

In this paper, we study the importance of object-centric modeling for unsupervised 3D object discovery. We propose the unsupervised discovery of Object-Centric neural Fields (uOCF) to instantiate this concept. To evaluate our approach, we collect three challenging new datasets, each with scenes containing objects of multiple categories set against complex backgrounds. Our results indicate that our object-centric design and the object-centric prior learning can substantially improve the systematic generalizability of unsupervised object discovery.

Acknowledgments. This work is in part supported by NSF RI #2211258, ONR MURI N00014-22-1-2740, ONR YIP N00014-24-1-2117, the Samsung Global Research Outreach (GRO) program, Amazon, and Google.

References

Barron, J. T., Mildenhall, B., Tancik, M., Hedman, P., Martin-Brualla, R., and Srinivasan, P. P. Mip-nerf: A multiscale representation for anti-aliasing neural radiance fields. In *ICCV*, 2021. 14

Biza, O., van Steenkiste, S., Sajjadi, M. S., Elsayed, G. F., Mahendran, A., and Kipf, T. Invariant slot attention: Object discovery with slot-centric reference frames. In *ICML*, 2023. 2, 4

Burgess, C. P., Matthey, L., Watters, N., Kabra, R., Higgins, I., Botvinick, M., and Lerchner, A. Monet: Unsupervised scene decomposition and representation. *arXiv:1901.11390*, 2019. 2

Cen, J., Fang, J., Yang, C., Xie, L., Zhang, X., Shen, W., and Tian, Q. Segment any 3d gaussians. *arXiv:2312.00860*, 2023a. 3

Cen, J., Zhou, Z., Fang, J., Shen, W., Xie, L., Zhang, X., and Tian, Q. Segment anything in 3d with nerfs. In *NeurIPS*, 2023b. 3

Chattpadhyay, P., Balaji, Y., and Hoffman, J. Learning to balance specificity and invariance for in and out of domain generalization. In *ECCV*, 2020. 1

Chen, C., Deng, F., and Ahn, S. Learning to infer 3d object models from images. *arXiv:2006.06130*, 2020. 2

Chen, H., Venkatesh, R., Friedman, Y., Wu, J., Tenenbaum, J. B., Yamins, D. L., and Bear, D. M. Unsupervised segmentation in real-world images via spelke object inference. In *ECCV*, 2022. 14

Collins, J., Goel, S., Deng, K., Luthra, A., Xu, L., Gundogdu, E., Zhang, X., Yago Vicente, T. F., Dideriksen, T., Arora, H., Guillaumin, M., and Malik, J. Abo: Dataset and benchmarks for real-world 3d object understanding. In *CVPR*, 2022. 5, 13

Crawford, E. and Pineau, J. Spatially invariant unsupervised object detection with convolutional neural networks. In *AAAI*, 2019. 2

Deng, W., Gould, S., and Zheng, L. On the strong correlation between model invariance and generalization. In *NeurIPS*, 2022. 1

Didolkar, A., Goyal, A., and Bengio, Y. Cycle consistency driven object discovery. *arXiv:2306.02204*, 2023. 2

Engelcke, M., Kosirek, A. R., Jones, O. P., and Posner, I. Genesis: Generative scene inference and sampling with object-centric latent representations. *arXiv:1907.13052*, 2019. 2

Eslami, S., Heess, N., Weber, T., Tassa, Y., Szepesvari, D., Kavukcuoglu, K., and Hinton, G. E. Attend, infer, repeat: Fast scene understanding with generative models. In *NeurIPS*, 2016. 2

Eslami, S. A., Rezende, D. J., Besse, F., Viola, F., Morcos, A. S., Garnelo, M., Ruderman, A., Rusu, A. A., Danihelka, I., Gregor, K., et al. Neural scene representation and rendering. *Science*, 2018. 2

Fan, Z., Wang, P., Jiang, Y., Gong, X., Xu, D., and Wang, Z. Nerf-sos: Any-view self-supervised object segmentation on complex scenes. *arXiv:2209.08776*, 2022. 3

Ge, Y., Yu, H.-X., Zhao, C., Guo, Y., Huang, X., Ren, L., Itti, L., and Wu, J. 3d copy-paste: Physically plausible object insertion for monocular 3d detection. *Neurips*, 2023. 4, 12

Grauman, K. and Darrell, T. Unsupervised learning of categories from sets of partially matching image features. In *CVPR*, 2006. 2

Greff, K., Rasmus, A., Berglund, M., Hao, T. H., Schmidhuber, J., and Valpola, H. Tagger: Deep unsupervised perceptual grouping. In *NeurIPS*, 2016. 2

Greff, K., Van Steenkiste, S., and Schmidhuber, J. Neural expectation maximization. In *NeurIPS*, 2017. 2

Greff, K., Kaufman, R. L., Kabra, R., Watters, N., Burgess, C., Zoran, D., Matthey, L., Botvinick, M., and Lerchner, A. Multi-object representation learning with iterative variational inference. In *ICML*, 2019. 2

Jia, B., Liu, Y., and Huang, S. Improving object-centric learning with query optimization. In *ICLR*, 2023. 1, 2, 6, 7, 17

Jiang, J., Janghorbani, S., de Melo, G., and Ahn, S. Scalor: Generative world models with scalable object representations. In *ICLR*, 2020. 2

Johnson, J., Alahi, A., and Fei-Fei, L. Perceptual losses for real-time style transfer and super-resolution. In *ECCV*, 2016. 5

Johnson, J., Hariharan, B., Van Der Maaten, L., Fei-Fei, L., Lawrence Zitnick, C., and Girshick, R. Clevr: A diagnostic dataset for compositional language and elementary visual reasoning. In *CVPR*, 2017. 6

Joulin, A., Bach, F., and Ponce, J. Discriminative clustering for image co-segmentation. In *CVPR*, 2010. 2

Kosiorek, A. R., Kim, H., Posner, I., and Teh, Y. W. Sequential attend, infer, repeat: Generative modelling of moving objects. In *NeurIPS*, 2018. 2

Kundu, A., Li, Y., and Rehg, J. M. 3d-rcnn: Instance-level 3d object reconstruction via render-and-compare. In *CVPR*, 2018. 2

Li, B., Sun, Z., Li, Q., Wu, Y., and Hu, A. Group-wise deep object co-segmentation with co-attention recurrent neural network. In *CVPR*, 2019. 2

Liang, S., Liu, Y., Wu, S., Tai, Y.-W., and Tang, C.-K. On-erf: Unsupervised 3d object segmentation from multiple views. *arXiv:2211.12038*, 2022. 2

Lin, Z., Wu, Y.-F., Peri, S. V., Sun, W., Singh, G., Deng, F., Jiang, J., and Ahn, S. Space: Unsupervised object-oriented scene representation via spatial attention and decomposition. In *ICLR*, 2020. 2

Locatello, F., Weissenborn, D., Unterthiner, T., Mahendran, A., Heigold, G., Uszkoreit, J., Dosovitskiy, A., and Kipf, T. Object-centric learning with slot attention. In *NeurIPS*, 2020. 2, 4

Mildenhall, B., Srinivasan, P. P., Tancik, M., Barron, J. T., Ramamoorthi, R., and Ng, R. Nerf: Representing scenes as neural radiance fields for view synthesis. In *ECCV*, 2020. 3

Monnier, T., Vincent, E., Ponce, J., and Aubry, M. Unsupervised layered image decomposition into object prototypes. In *ICCV*, 2021. 2

Müller, N., Simonelli, A., Porzi, L., Bulo, S. R., Nießner, M., and Kortschieder, P. Autorf: Learning 3d object radiance fields from single view observations. In *CVPR*, 2022. 2

Nguyen-Phuoc, T. H., Richardt, C., Mai, L., Yang, Y., and Mitra, N. Blockgan: Learning 3d object-aware scene representations from unlabelled images. In *NeurIPS*, 2020. 3

Niemeyer, M. and Geiger, A. Giraffe: Representing scenes as compositional generative neural feature fields. In *CVPR*, 2021. 3

Oquab, M., Dariseti, T., Moutakanni, T., Vo, H., Szafraniec, M., Khalidov, V., Fernandez, P., Haziza, D., Massa, F., El-Nouby, A., et al. Dinov2: Learning robust visual features without supervision. *arXiv:2304.07193*, 2023. 3

Ost, J., Mannan, F., Thuerey, N., Knodt, J., and Heide, F. Neural scene graphs for dynamic scenes. In *CVPR*, 2021. 2

Park, J. J., Florence, P., Straub, J., Newcombe, R., and Lovegrove, S. Deepsdf: Learning continuous signed distance functions for shape representation. In *CVPR*, 2019. 3

Ramakrishnan, S. K., Gokaslan, A., Wijmans, E., Maksymets, O., Clegg, A., Turner, J., Undersander, E., Galuba, W., Westbury, A., Chang, A. X., et al. Habitat-matterport 3d dataset (hm3d): 1000 large-scale 3d environments for embodied ai. *arXiv:2109.08238*, 2021. 8, 18

Ranftl, R., Lasinger, K., Hafner, D., Schindler, K., and Koltun, V. Towards robust monocular depth estimation: Mixing datasets for zero-shot cross-dataset transfer. *TPAMI*, 2022. 14

Russell, B. C., Freeman, W. T., Efros, A. A., Sivic, J., and Zisserman, A. Using multiple segmentations to discover objects and their extent in image collections. In *CVPR*, 2006. 2

Sajjadi, M. S., Duckworth, D., Mahendran, A., van Steenkiste, S., Pavetic, F., Lucic, M., Guibas, L. J., Greff, K., and Kipf, T. Object scene representation transformer. In *NeurIPS*, 2022. 2, 14

Sitzmann, V., Zollhöfer, M., and Wetzstein, G. Scene representation networks: Continuous 3d-structure-aware neural scene representations. In *NeurIPS*, 2019. 3

Sivic, J., Russell, B. C., Efros, A. A., Zisserman, A., and Freeman, W. T. Discovering objects and their location in images. In *ICCV*, 2005. 2

Smith, C., Yu, H.-X., Zakharov, S., Durand, F., Tenenbaum, J. B., Wu, J., and Sitzmann, V. Unsupervised discovery and composition of object light fields. *TMLR*, 2023. 1, 2, 6, 7

Spelke, E. S. Principles of object perception. *Cognitive science*, 1990. 14

Stelzner, K., Kersting, K., and Kosiorek, A. R. Decomposing 3d scenes into objects via unsupervised volume segmentation. *arXiv:2104.01148*, 2021. 1, 2

Tewari, A., Fried, O., Thies, J., Sitzmann, V., Lombardi, S., Sunkavalli, K., Martin-Brualla, R., Simon, T., Saragih, J., Nießner, M., et al. State of the art on neural rendering. *CGF*, 2020. 3

Vo, H. V., Pérez, P., and Ponce, J. Toward unsupervised, multi-object discovery in large-scale image collections. In *ECCV*, 2020. 2

Wang, G., Chen, Z., Loy, C. C., and Liu, Z. Sparsenerf: Distilling depth ranking for few-shot novel view synthesis. In *ICCV*, 2023a. 5

Wang, H., Sridhar, S., Huang, J., Valentin, J., Song, S., and Guibas, L. J. Normalized object coordinate space for category-level 6d object pose and size estimation. In *CVPR*, 2019. 4

Wang, Q., Wang, Y., Birsak, M., and Wonka, P. Blobgan-3d: A spatially-disentangled 3d-aware generative model for indoor scenes. *arXiv:2303.14706*, 2023b. 3

Wu, J., Tenenbaum, J. B., and Kohli, P. Neural scene de-rendering. In *CVPR*, 2017. 2

Wu, Q., Liu, X., Chen, Y., Li, K., Zheng, C., Cai, J., and Zheng, J. Object-compositional neural implicit surfaces. In *ECCV*, 2022. 3

Xie, Y., Takikawa, T., Saito, S., Litany, O., Yan, S., Khan, N., Tombari, F., Tompkin, J., Sitzmann, V., and Sridhar, S. Neural fields in visual computing and beyond. *CGF*, 2022. 3

Yang, B., Zhang, Y., Xu, Y., Li, Y., Zhou, H., Bao, H., Zhang, G., and Cui, Z. Learning object-compositional neural radiance field for editable scene rendering. In *CVPR*, 2021. 3

Yang, J., Pavone, M., and Wang, Y. Freenerf: Improving few-shot neural rendering with free frequency regularization. In *CVPR*, 2023. 5

Yao, S., Hsu, T. M. H., Zhu, J.-Y., Wu, J., Torralba, A., Freeman, W. T., and Tenenbaum, J. B. 3d-aware scene manipulation via inverse graphics. In *NeurIPS*, 2018. 2

Yu, A., Ye, V., Tancik, M., and Kanazawa, A. pixelnerf: Neural radiance fields from one or few images. In *CVPR*, 2021. 14

Yu, H.-X., Guibas, L. J., and Wu, J. Unsupervised discovery of object radiance fields. In *ICLR*, 2022. 1, 2, 6, 7, 12, 14, 17

Zhang, R. Making convolutional networks shift-invariant again. In *ICML*, 2019. 1

A Supplementary Document Overview

This supplementary document is structured as follows: We begin with the proof of concept in Appendix B and provide the implementation details in Appendix C. Then, we discuss the limitations of our approach in Appendix D and present additional experiments in Appendix E. For more results, please refer to our project page: <https://red-fairy.github.io/uOCF/>.

B Proof of Concept

We conduct a toy experiment (Figure 9) to demonstrate that our model has successfully learned object position, rotation, and scale. In this experiment, we begin with two images (input 1 and input 2) of a chair placed at the scene’s center, exhibiting different sizes (on the left) or rotation angles (on the right), all captured from the same viewing direction.

We extract the object latents from these images, interpolate them, and then send the interpolated latents to the decoder. As shown between the two input images, we observe a smooth transition in object size and rotation, indicating that the latent representation has effectively captured the scale and rotation of objects.

In the second row, we placed the chairs in different positions. As shown on the right, we obtained a smooth transition again, proving that our model could disentangle object positions from the latent representation.

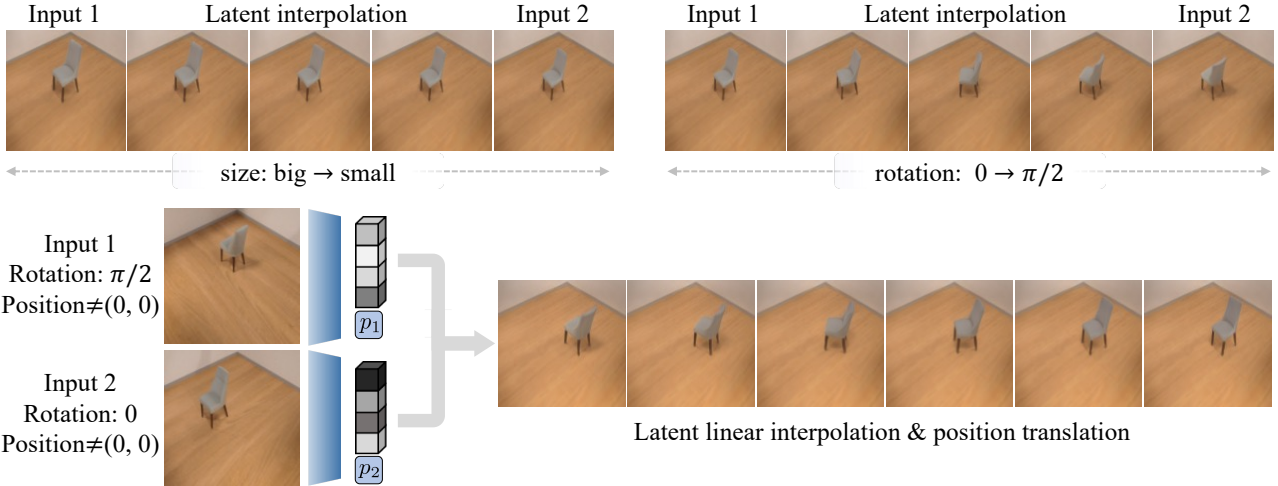


Figure 9: Proof of concept. We demonstrate that uOCF has effectively learned objects’ scale and orientation along with the translation-invariant object representation by interpolating the representation of two identical objects with different orientations and scales to obtain transitional results.

C Implementation

C.1 Model Architecture

Encoder. Our encoder module consists of a frozen DINO encoder and two convolutional layers. We illustrate its architecture in Figure 10(a).

Latent Extraction Module. While motivated by the background-aware slot attention module proposed by (Yu et al., 2022), our latent inference module exhibits three key differences: (1) The object queries are initialized with learnable embeddings instead of being sampled from learnable Gaussians, which enhances training stability; (2) We jointly extract object positions and their latent representations and add object-specific positional encoding to utilize the extracted position information; (3) We remove the Gated Recurrent Unit (GRU) and replace it with the transformer architecture to smooth the gradient flow.

When lifting the object image position $\mathbf{p}_i^{\text{img}}$ to the world coordinates, we consider two scenarios: (1) for objects on a known shared plane (*e.g.*, using plane detection (Ge et al., 2023)), a direct ray extension (extend the ray between the camera center and $\mathbf{p}_i^{\text{img}}$ to intersect the ground plane) is used (Figure 11, left); (2) we extend the rays by depth $d \cdot s_i$, where d is the distance between the camera and the scene center and $\{s_i\}_{i=1}^K$ are scaling terms predicted by a linear layer using the camera parameters and object latent as input (Figure 11, right). The two variants are denoted as uOCF-P and uOCF-N, respectively, and uOCF refers to uOCF-P by default.

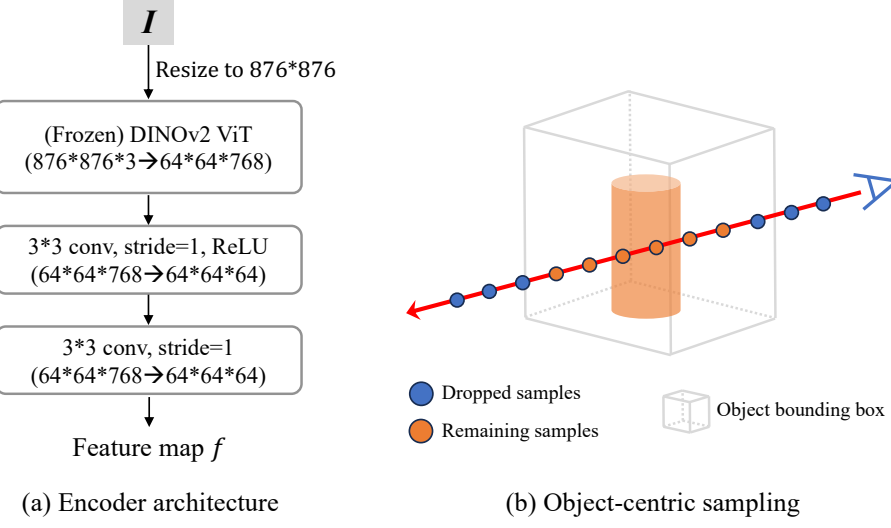


Figure 10: (a) Architecture of our encoder module. (b) Object-centric sampling: We drop the samples distant from the predicted object position for efficient sampling..

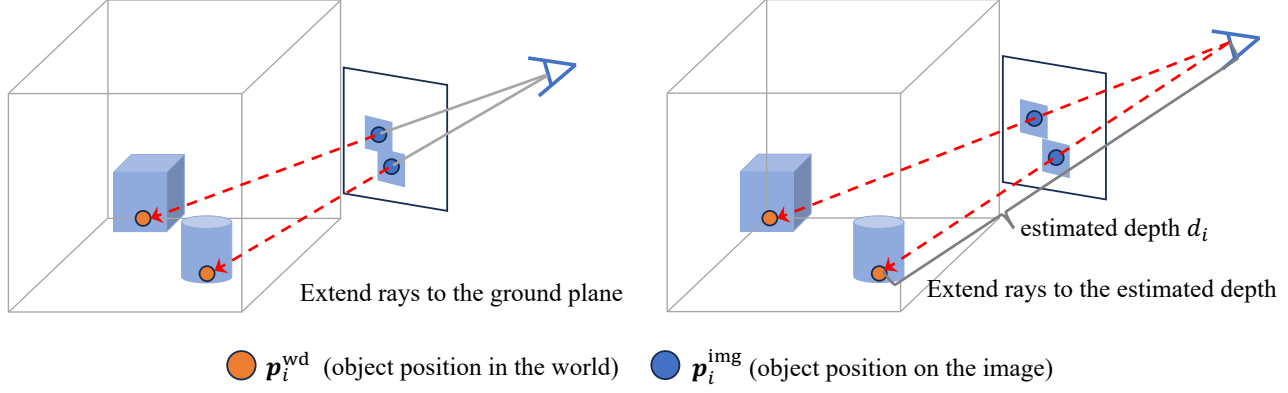


Figure 11: Lifting 2D position p_i^{img} to 3D position p_i^{wd} with (left) and without (right) ground plane assumption.

C.2 Data Collection

This section introduces the details of our datasets.

Room-Texture. In Room-Texture, objects are chosen from 324 ABO objects (Collins et al., 2022) from the “armchair” category. The single-object subset contains four scenes for each object instance, resulting in 1296 scenes in total. The multiple-object subset includes 5,000 scenes for training and 100 for evaluation, with each scene containing 2-4 objects set against a background randomly chosen from a collection of floor textures. Each scene is rendered from 4 directions toward the center.

Kitchen-Matte. In Kitchen-Matte, objects are diffuse and have no texture. The dataset comprises 16 objects and 6 tablecloths in total. We captured 3 images for each tabletop scene and 2 for each kitchen scene. This dataset contains 735 scenes for training and 102 for evaluation, each containing 3-4 objects. We calibrate the cameras using the OpenCV library.

Kitchen-Shiny. In Kitchen-Shiny, objects are specular, and the lighting is more complex. The dataset comprises 12 objects and 6 tablecloths, and the other settings are identical to Kitchen-Matte. This dataset contains 324 scenes for training and 56 for evaluation, each containing 4 objects.

C.3 Training Configuration

This section discusses the training configuration of uOCF.

We employ Mip-NeRF (Barron et al., 2021) as our NeRF backbone and estimate the depth maps by MiDaS (Ranftl et al., 2022). An Adam optimizer with default hyper-parameters and an exponential decay scheduler is used across all experiments. The initial learning rate is 0.0003 for the first stage and 0.00015 for the second stage. Loss weights are set to $\lambda_{\text{perc}} = 0.006$, $\lambda_{\text{depth}} = 1.5$, and $\lambda_{\text{occ}} = 0.1$. The position update momentum m is set to 0.5, and the latent inference module lasts $T = 6$ iterations.

Coarse-To-Fine Progressive Training. We employ a coarse-to-fine strategy in our second training stage to facilitate training at higher resolutions. Reference images are downsampled to a lower resolution (64×64) during the coarse training stage and replaced by image patches with the same size as the low-resolution images randomly cropped from the high-resolution (128×128) input images during the fine training stage.

Locality Constraint and Object-Centric Sampling. We employ the locality constraint (a bounding box for foreground objects in the world coordinate) proposed by Yu et al. (2022) in both training stages but only adopt it before starting object-centric sampling. The number of samples along each ray before and after starting object-centric sampling is set to 64 and 256, respectively. We provide an illustration of our object-centric sampling strategy in Figure 10(b).

Training Configuration on Room-Texture. During stage 1, we train the model for 100 epochs directly on images of resolution 128×128 . We start with the reconstruction loss only, add the perceptual 10th epoch, and start the object-centric sampling at the 20th epoch. During stage 2, we train the model for 60 epochs on the coarse stage and another 60 on the fine stage. We start with the reconstruction loss only, add the perceptual loss at the 10th epoch, and start the object-centric sampling from the 20th epoch.

Training Configuration on Kitchen-Matte and Kitchen-Shiny. Both kitchen datasets share the same training configuration with Room-Texture in stage 1. During stage 2, we train the model for 750 epochs, where the fine stage starts at the 250th epoch. We add the perceptual loss at the 50th epoch and start the object-centric sampling from the 150th epoch.

D Limitations Analysis

Limitation on Reconstruction Quality. Scene-level generalizable NeRFs (Yu et al., 2021; Sajjadi et al., 2022; Yu et al., 2022) commonly face challenges in accurately reconstructing detailed object textures. To address this limitation, we adopted the MipNeRF (Barron et al., 2021) backbone and included the depth and occlusion regularizers. However, despite these enhancements, our approach still encounters difficulty capturing extremely high-frequency details. As shown in Figure 12(a), our method fails to replicate the mug’s detailed texture. Future research may benefit from exploring more advanced NeRF backbones to further improve texture detail reconstruction.

Failure in Position Prediction. Our two-stage training pipeline, despite its robustness in many situations, is not immune to errors, particularly in object position prediction. Due to the occlusion between objects, using the attention-weighted mean for determining object positions can sometimes lead to inaccuracies. Although a bias term can rectify this in most instances (Figure 6), discrepancies persist under a few conditions, as depicted in Figure 12(b).

E Additional Experiments

E.1 Ablation Studies

Training Pipeline. We first justify the efficacy of our two-stage object-centric prior learning pipeline. Heuristically, the first stage involves learning the fundamentals of object-centric NeRFs, such as the physical coherence (Spelke, 1990) property—a crucial aspect in unsupervised segmentation (Chen et al., 2022). The model then utilizes the learned object prior in the subsequent training stage on complex real-world scenes.

We note that although the objects in the two datasets might share a large domain gap, the learned object priors are transferable. The main paper already presents the model’s adaptability from synthetic chairs to actual dinnerware. To further validate this concept, we consider using the simple CLEVR shapes (balls, cubes, and cylinders) for object prior learning, which maintains fairly good results, as shown in Table 4.

As illustrated in Table 4 and Figure 13, omitting the object prior learning stage leads to the model incorrectly associating some foreground objects with the background, yielding poorer results. Excluding the depth and occlusion losses significantly hampers the visual quality, resulting in a performance decline. We also present results from eliminating the object-centric sampling strategy, which slightly impacts the overall reconstruction quality. We also tried learning object prior from multi-object Room-Texture, which provides even better results, possibly because the two datasets share the maximum

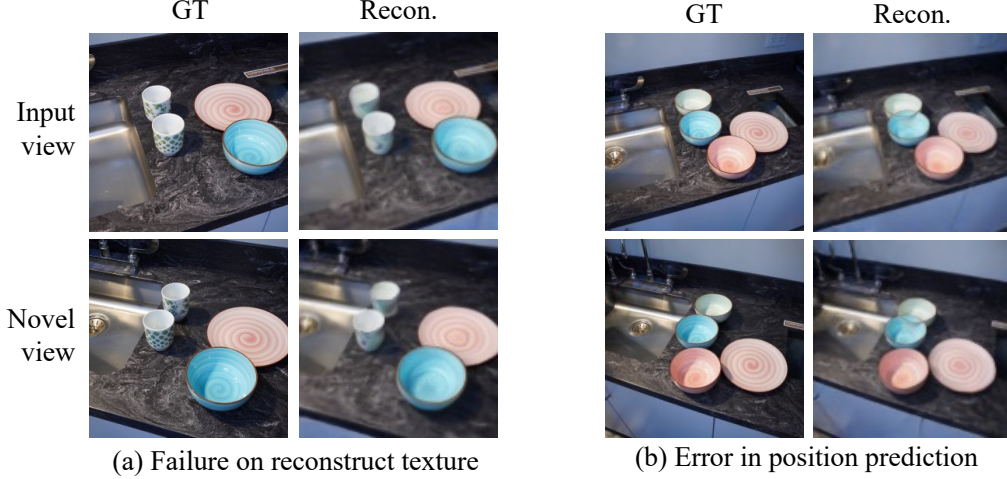


Figure 12: Failure case visualizations. Our method may fail to reconstruct intricate object texture or predict biased object position.

number of objects in the scene.

Table 4: Ablation study for the training pipeline on Kitchen-Shiny.

Method	PSNR↑	SSIM↑	LPIPS↓
w/o object-centric prior learning	26.81	0.806	0.125
Learn object prior from CLEVR	27.96	0.840	0.074
w/o object-centric sampling	27.31	0.852	0.072
w/o ℓ_{depth} and ℓ_{occ}	26.79	0.819	0.081
Learn object prior from single-object Room-Texture (uOCF)	28.58	0.862	0.049
Learn object prior from multi-object Room-Texture	29.58	0.878	0.037

Encoder Design. We ablate the encoder design to prove that simply substituting the shallow encoder in previous methods is inadequate for unsupervised object discovery in complex real-world scenes. As shown by the qualitative results in Table 5 and quantitative results in 17, simply integrating DINO fails to address the limitations of existing methods in complex real-world scenes.

Table 5: Ablation study for different encoder designs on Kitchen-Shiny. uORF-DINO modifies the standard uORF by replacing its shallow U-Net encoder with the DINO encoder.

Method	Novel view synthesis		
	PSNR↑	SSIM↑	LPIPS↓
uORF	19.23	0.602	0.336
uORF-DINO	21.06	0.662	0.282
uOCF (ours)	28.58	0.862	0.049

E.2 Discussion on the Number of Object Queries

The above experiments are conducted on scenes with 2-4 objects for training and evaluation, with the number of object queries K (*i.e.*, the maximum number of objects supported) all set to 4. This section further explores the effect of varying K , particularly exploring scenarios where K surpasses the upper limit of objects present in the scene.

The quantitative results in Table 6 and qualitative results in Figure 14 indicate the robustness of our framework to variations in the number of object queries K . Notably, when K is set higher than the actual count of objects in a scene, certain object

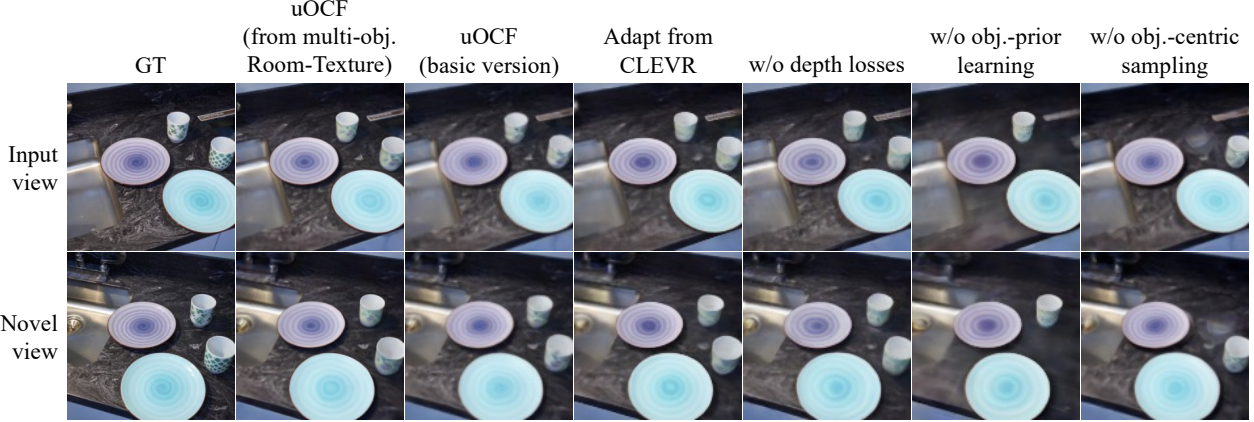


Figure 13: Qualitative ablation study for the training pipeline on Kitchen-Shiny. Removing either object-centric training strategies or removing the regularizations significantly impairs the visual quality and may even make the model fail to discover all objects in the scene.

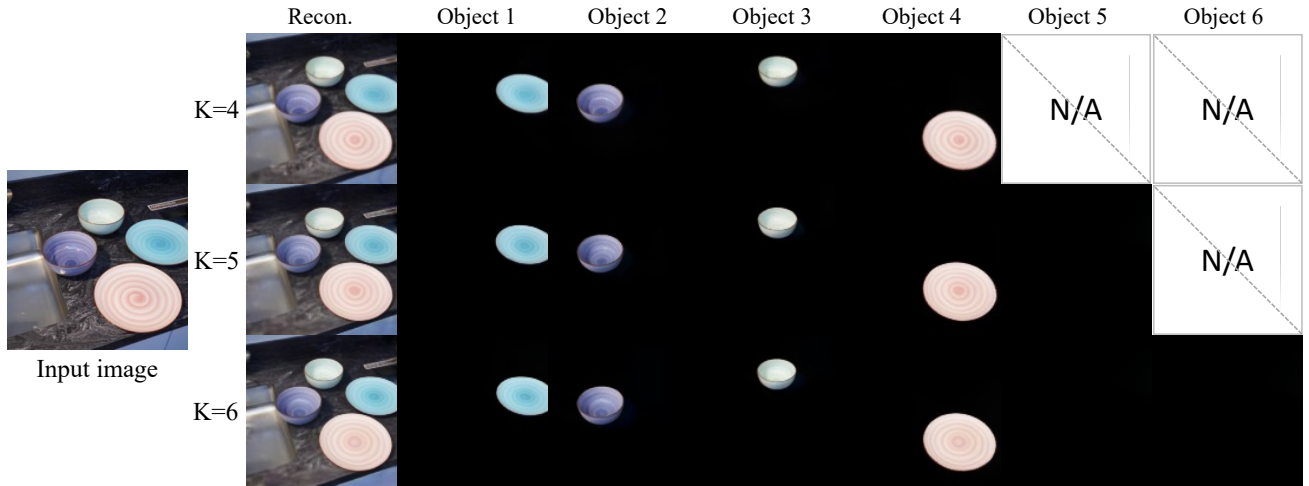


Figure 14: Qualitative results of uOCF on scenes with larger object queries K . The order of the object reconstructions is rearranged for better visualization.

queries yield empty reconstructions. This phenomenon highlights uOCF’s adaptability to complex scenes, *i.e.*, adjusting its output in response to the excess capacity represented by the larger K value.

E.3 Generalizability: Few-Shot and Zero-shot Object Discovery

Extending the discussions from Sec. 4.4, this section delves into the generalizability of uOCF. In contrast to previous experiments that utilized the full Kitchen-Shiny dataset for training, we now consider a more challenging scenario, where the model is trained with a limited number of scenes—specifically, 10, 50, or 100—and then tested on unseen scenes.

Figure 15 illustrates a notable trend: the reconstruction quality of uOCF deteriorates in correlation with the reduction in the number of training scenes. Particularly, with an extremely limited training set, the model struggles to differentiate objects from the background. This underscores the significance of the dataset size for effective unsupervised object discovery.

Sec. 4.4 also provides experiments on adapting from Room-Texture to HM3D (a scanned indoor scene dataset) with test-time optimization. To further understand our approach, we provide the direct inference results (*i.e.*, without test-time optimization) in Figure 16. As shown, our method can accurately identify and segment the chair instances in the scene and deliver plausible reconstruction results.

Table 6: Quantitative novel view synthesis result Kitchen-Shiny with a larger number of object queries K .

Method	PSNR \uparrow	SSIM \uparrow	LPIPS \downarrow
$K = 4$	28.58	0.862	0.049
$K = 5$	28.28	0.846	0.059
$K = 6$	28.04	0.848	0.058

E.4 Additional Qualitative Results

Scene Decomposition Visualizations. We first present the scene decomposition results for our scene manipulation experiment (Sec. 4.3) in Figure 17. Notably, uORF (Yu et al., 2022) puts all objects within the background, whereas BO-QSA (Jia et al., 2023) binds the same object to all queries, resulting in identical foreground reconstruction. Contrasting these, uOCF accurately differentiates between the foreground objects and the background.

Scene Segmentation Visualizations. Afterward, we provide scene segmentation results on the kitchen datasets in Figure 18. Unlike compared methods that yield cluttered results, uOCF consistently yields high-fidelity segmentation results.

Novel View Synthesis Visualizations. Finally, we offer more qualitative results for novel view synthesis in Figures 18, 19, and 20. Our method produces much better results than compared methods regarding visual quality.

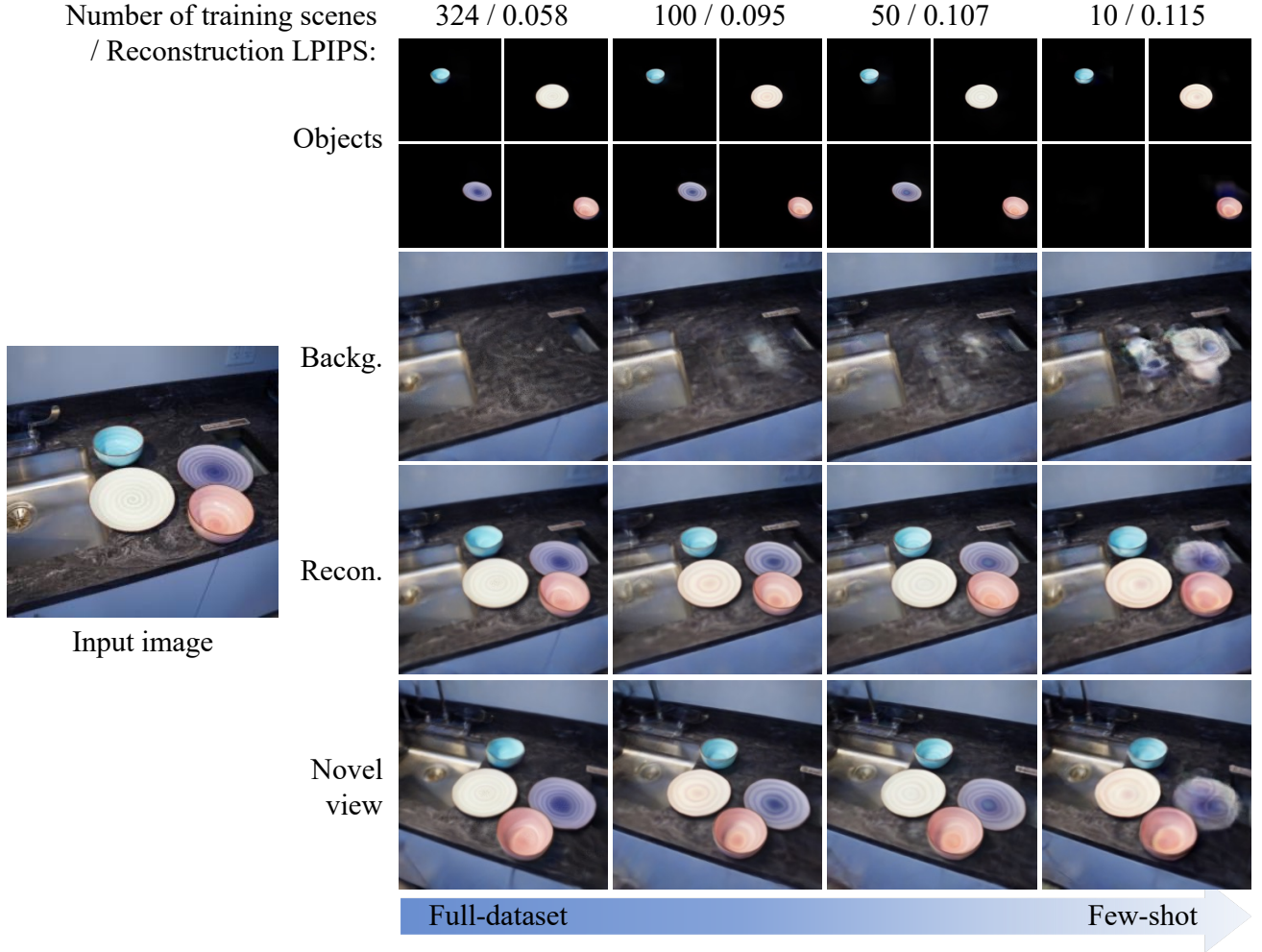


Figure 15: Ablation study on the few-shot settings, *i.e.*, decrease the number of scenes available during training. The order of the object reconstructions is rearranged for better visualization, and the LPIPS values are computed between images of resolution 256×256 .

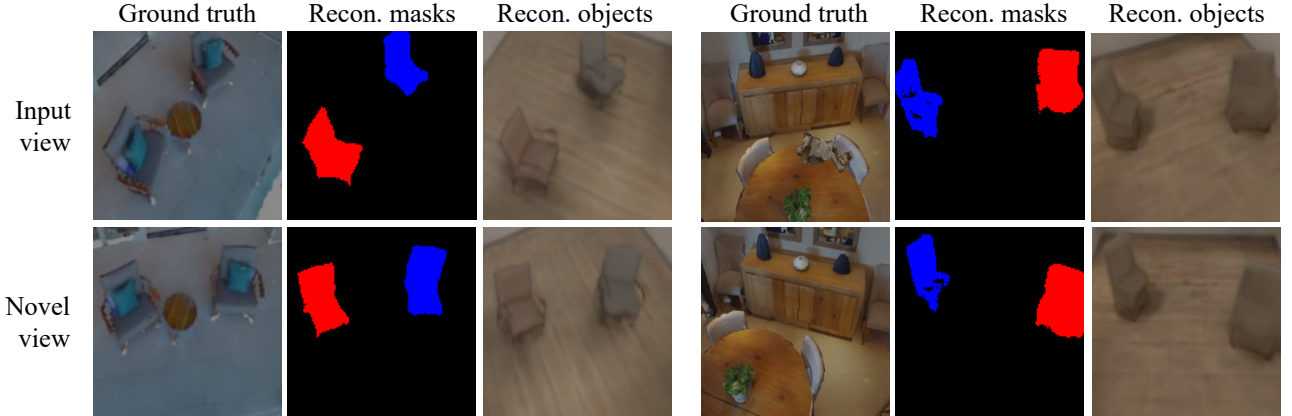


Figure 16: Zero-shot inference on the HM3D (Ramakrishnan et al., 2021) dataset. Our method can discover and segment the object instances belonging to the categories it has seen during training from the scene and deliver plausible reconstruction results.

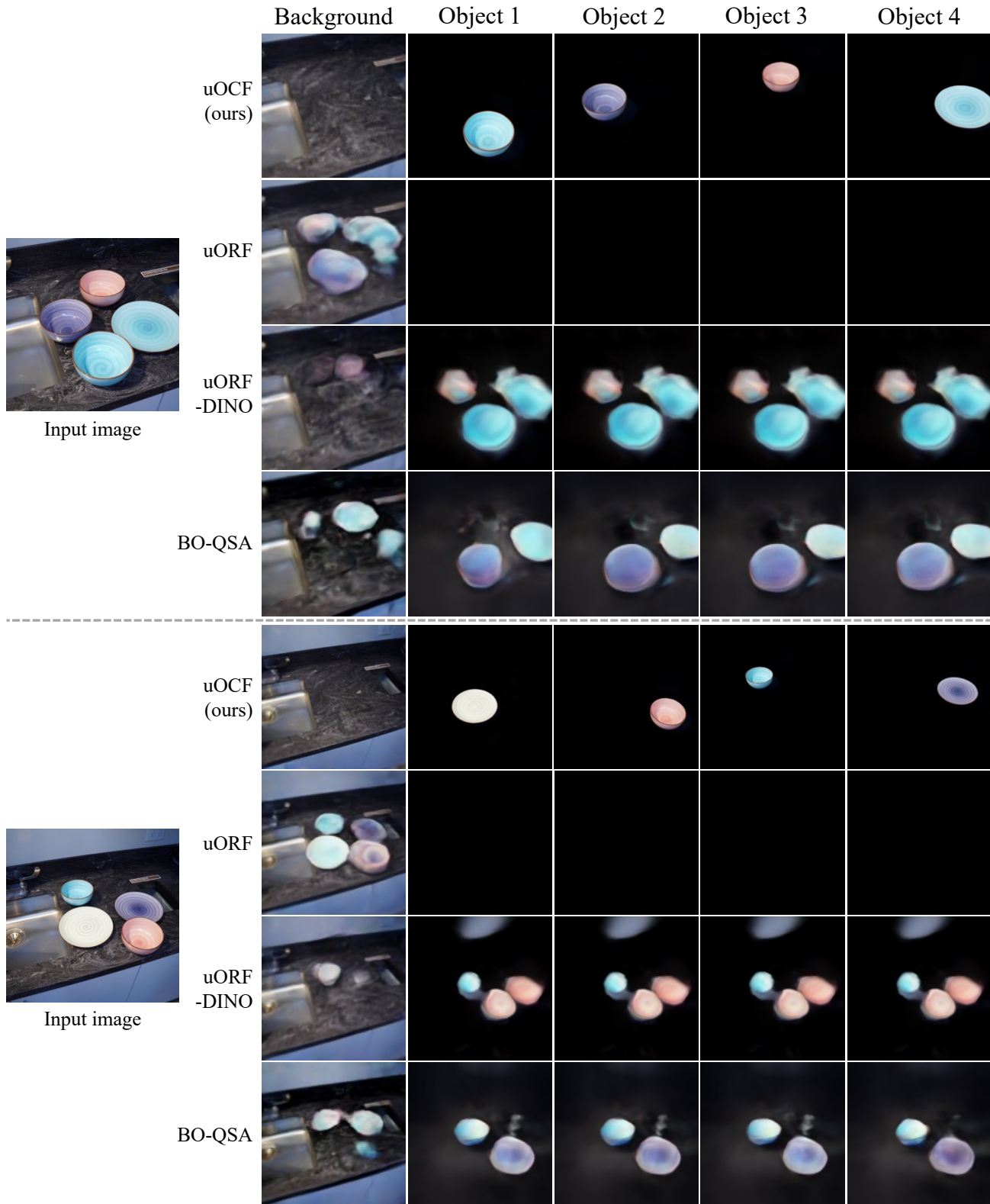


Figure 17: Scene decomposition reconstruction comparison results on Kitchen-Shiny. We rearranged the order of the object reconstructions for better visualization.

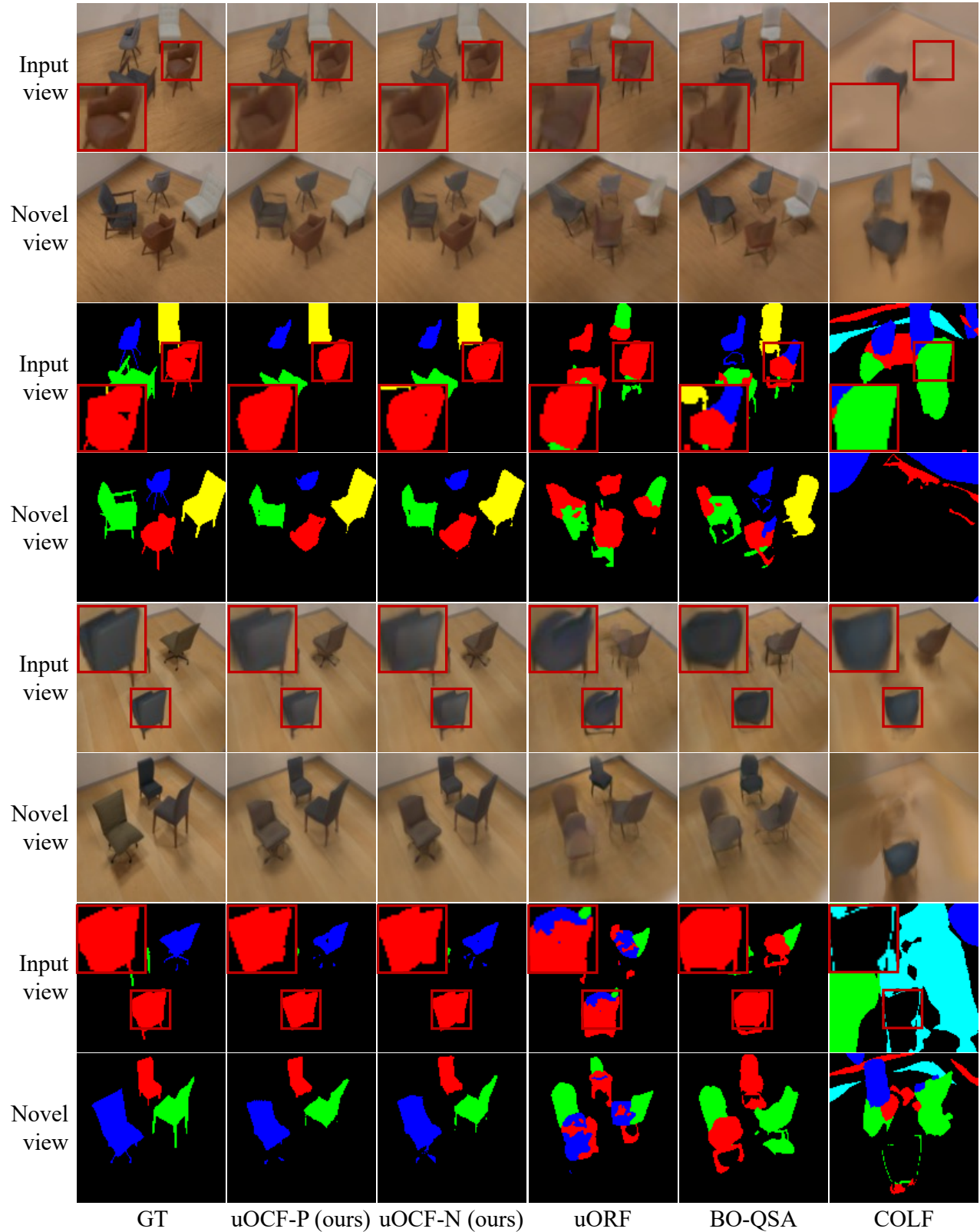


Figure 18: Additional qualitative comparison results on the Room-Texture dataset.

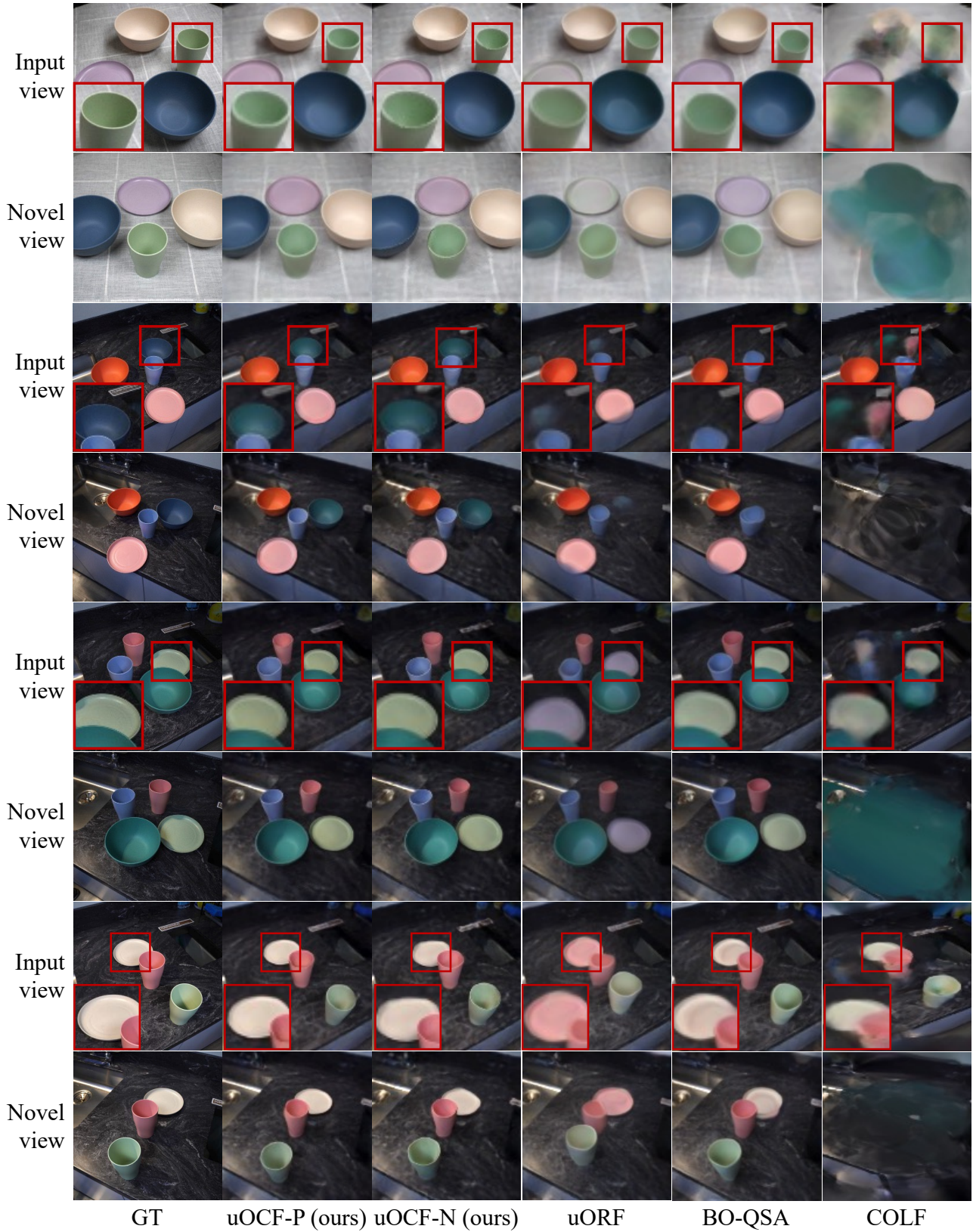


Figure 19: Additional qualitative results on the Kitchen-Matte dataset.

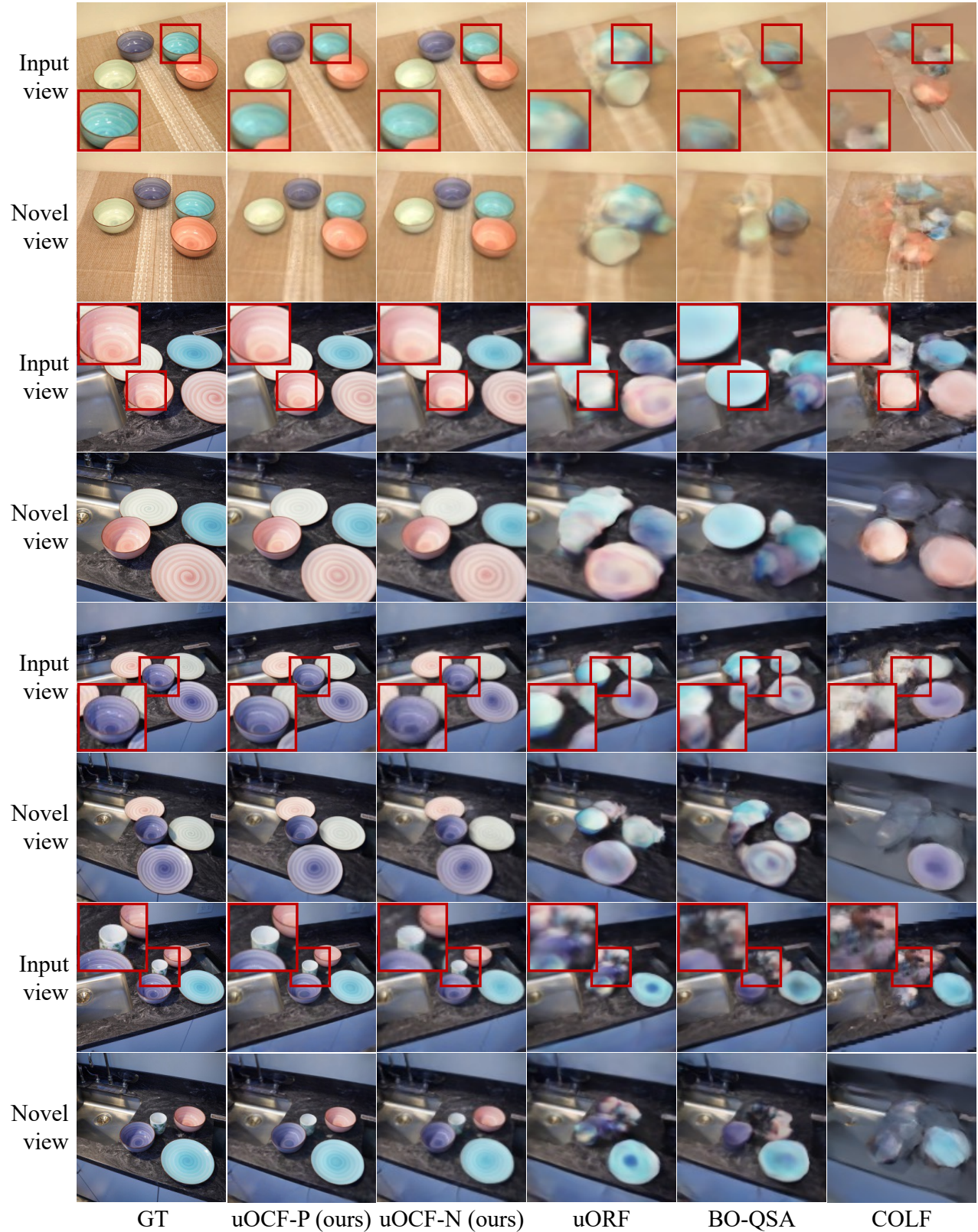


Figure 20: Additional qualitative comparison results on the Kitchen-Shiny dataset.